research papers

Crystal design by CH···N and N···N interactions: high-pressure structures of high-nitrogen-content azido-triazolopyridazines compounds

Anna Olejniczak,[a]* Anna Katrusiak,[b] Marcin Podsiadło[a] and Andrzej Katrusiak[a]*

[a]Faculty of Chemistry, Adam Mickiewicz University, Uniwersytetu Poznańskiego 8, Poznań, 61-614, Poland, and [b]Department of Organic Chemistry, Poznan University of Medical Sciences, Grunwaldzka 6, Poznań, 60-780, Poland. *Correspondence e-mail: aniao@amu.edu.pl, katran@amu.edu.pl

High-nitrogen-content compounds 6-azido-1,2,4-triazolo[4,3-b]pyridazine ($C_5H_3N_7$) and its 3-methyl derivative ($C_6H_5N_7$) have been *in situ* crystallized in a diamond-anvil cell and their structures determined by single-crystal X-ray diffraction. Under ambient and high-pressure conditions the crystallizations yield the same phases: the $C_5H_3N_7$ anhydrate and $C_6H_5N_7$ hydrated clathrate. In both the structures there are clearly distinguished regions of short CH···N and N···N intermolecular contacts, the latter involving exclusively the azide groups. High pressure initially increases the contents of water in the channel pores of the clathrate.

1. Introduction

Triazolopyridazine and azide groups are present in many high-nitrogen content compounds, which are widely applied for various purposes, for example as energetic materials and active pharmaceutical ingredients (Katrusiak *et al.*, 1996, 2005; Bałoniak & Katrusiak, 1994; Yang *et al.*, 2015; Olejniczak *et al.*, 2019). It is characteristic that such high-nitrogen organic compounds have relatively high density, despite the absence of strong intermolecular contacts in their structures (Bernstein, 2002; Fabbiani & Pulham, 2006; Millar *et al.*, 2010; Seryotkin *et al.*, 2016; Zakharov *et al.*, 2017; Gatta *et al.*, 2018; Gaydamaka *et al.*, 2019). The high density can be associated with a small content of H atoms, however, there is no systematic information about the aggregation types and intermolecular interactions. The CH groups are expected to engage in C—H···N hydrogen bonds, while the excess of other N atoms – potential H-atom acceptors – would either be redirected into separate regions of N···N contacts in the structure (Olejniczak *et al.*, 2019) or would find H-atom donors by favoring the crystallization in the form of solvates or host–guest compounds. Varied thermodynamic conditions can significantly change the crystal structure and conformations of compounds, as well as their composition and reactivity (Fabbiani & Pulham, 2006; Boldyreva, 2008, 2014; Resnati *et al.*, 2015). In order to provide new information about the aggregation of high-N-content molecules, we have investigated the structures of two azido-triazolopyridazine compounds: 6-azido-1,2,4-triazolo[4,3-b]pyridazine, $C_5H_3N_7$ (m.p. 438 K) and its methyl derivative, $C_6H_5N_7$ (m.p. 400 K). In the solid state both these compounds are present as the azide tautomers, although they can also transform into the
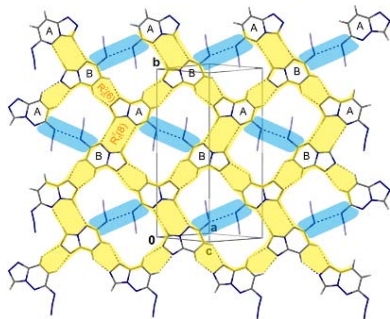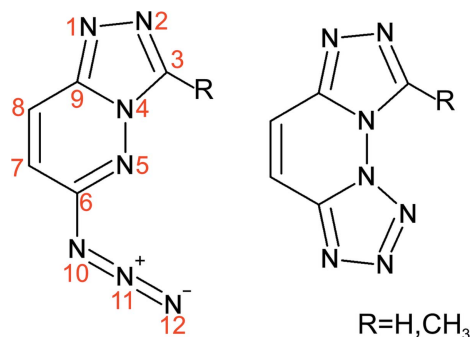
Figure 1
Structural formula of 6-azido-1,2,4-triazolo[4,3-*b*]pyridazine ($C_5H_3N_7$) and its 3-methyl derivative ($C_6H_5N_7$) (left-hand view) and their tetrazole tautomer (right-hand view).

tetrazole form (Fig. 1). In order to check the stability of the structures obtained under ambient conditions, we have recrystallized these two compounds under high pressure. Additionally, low temperature has been employed for comparing the effects of thermal expansion and compressibility on intermolecular contacts in $C_6H_5N_7$ clathrate.

2. Experimental

High-pressure recrystallizations of compounds $C_5H_3N_7$ and $C_6H_5N_7$ were performed from the saturated acetone or aqueous solution in the diamond anvil cell (DAC) (Merrill & Bassett, 1974). Several small sample crystals were loaded to the DAC chamber, then filled with the saturated solution, because its concentration at room temperature was too low to obtain single crystals sufficiently large for X-ray diffraction measurements. After increasing the pressure all crystals were dissolved by heating the sample, so the concentration was

considerably increased and then a single crystal was grown by slowly cooling the DAC.

6-Azido-1,2,4-triazolo[4,3-*b*]pyridazine ($C_5H_3N_7$): several solvents were tried for the recrystallization and the best results were obtained from acetone or aqueous solutions. Three series of experiments were performed. In the first series the acetone solution was used for growing a single crystal at 0.1 GPa and its X-ray diffraction data were collected. Then the pressure was increased in small steps under isothermal conditions and after each step the diffraction data were measured [Fig. 2(*a*)]. At 1.38 GPa the acetone crystallized, which hampered the further hydrostatic compression. In the second series also the acetone solution was used [Fig. 2(*b*)], but the isochoric recrystallization was performed after each pressure increase. Above 1.20 GPa acetone crystallized. The last analogous series of experiments was carried out for the aqueous solution [Figs. 2(*c*)–2(*d*)].

6-Azido-3-methyl-1,2,4-triazolo[4,3-*b*]pyridazine ($C_6H_5N_7$): single crystals, large enough for X-ray diffraction, could be recrystallized only from the aqueous solution and only in the pressure range up to 0.75 GPa (Fig. 3). The methanol, acetone or ethanol solutions led to polycrystals or very small crystals. The main difficulty in obtaining a single crystal was due to persistent nucleation of other competing seeds. The crystals obtained at high pressure could be recovered after releasing the pressure (Fig. 3) and their structure was determined at ambient pressure as a function of temperature, too. The water occupancy in $C_6H_5N_7 \cdot xH_2O$ hydrates refined to 0.3 at 0.1 MPa;
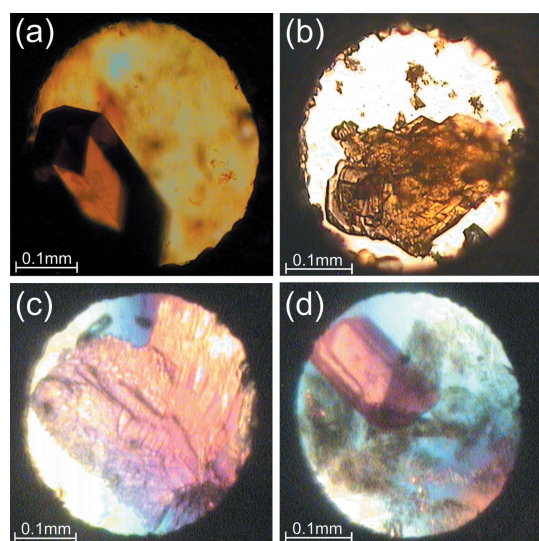

Figure 2
Single crystals of $C_5H_3N_7$ obtained from different high-pressure recrystallizations: (*a*) at 0.20 GPa (viewed in polarized light) and (*b*) at 0.85 GPa, both from the acetone solution; (*c*) at 0.14 GPa and (*d*) at 1.02 GPa, both from aqueous solution and viewed in polarized light.
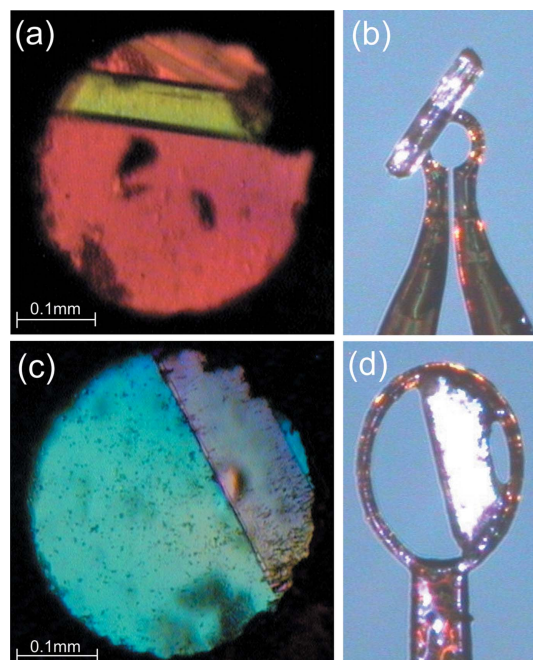

Figure 3
Single crystals of $C_6H_5N_7 \cdot xH_2O$: (*a*) *in situ* crystallized from the aqueous solution at 0.10 GPa/296 K viewed in polarized light; (*b*) the sample recovered from the chamber after the compression to 0.74 GPa; (*c*) the single crystal grown at 0.23 GPa/296 K (in polarized light) and (*d*) the recovered sample stuck in a nylon loop.

Table 1
Selected data of $C_5H_3N_7$ and $C_6H_5N_7 \cdot xH_2O$ recrystallized from the aqueous solutions (see Tables S1–S3).

Compound	$C_5H_3N_7$	$C_5H_3N_7$	$C_6H_5N_7 \cdot 0.3H_2O$	$C_6H_5N_7 \cdot 0.5H_2O$
p (GPa)	0.14 (2)	1.40 (2)	0.0001	0.58 (2)
Space group	$P2_1/c$	$P2_1/c$	$I4_1/a$	$I4_1/a$
a (Å)	8.1016 (19)	7.7755 (16)	28.1674 (5)	27.972 (6)
b (Å)	18.473 (4)	18.017 (3)	28.1674 (5)	27.972 (6)
c (Å)	9.04 (2)	8.75 (3)	4.15209 (11)	3.9991 (8)
β (°)	95.91 (6)	93.53 (9)		
Volume (Å^3)	1346 (3)	1224 (4)	3294.29 (14)	3129.1 (14)
Z, Z'	8, 2	8, 2	16, 1	16, 1
D_{calc} (g cm^{-3})	1.590	1.749	1.451	1.555
Final R_1, wR_2 ($I > 2\sigma_1$)	0.0587, 0.0608	0.0775, 0.1640	0.0371, 0.1033	0.0843, 0.1658

to 0.4 at 0.1 MPa and from 275 K to 100 K; to 0.5 at 0.10 GPa/296 K and 0.58 GPa/296 K; and to 0.6 at 0.23 GPa/296 K.

Pressure in the DAC chamber was calibrated by the ruby-fluorescence method (Piermarini *et al.*, 1975; Mao *et al.*, 1985) with a Photon Control spectrometer affording an accuracy of 0.02 GPa; the calibration was performed before and after the diffraction measurements.

The crystal sample in the DAC was centered on the diffractometer by the gasket shadowing method (Budzianowski & Katrusiak, 2004). For the low-temperature measurements, an Oxford Cryosystems 700 Series attachment and SuperNova diffractometer using Cu $K\alpha$ radiation and CCD plate Atlas detector were used. The high-pressure diffraction data were measured with a KUMA KM4-CCD diffractometer using Mo $K\alpha$ radiation and CCD plate Eos

detector. *CrysAlisPro* (version 171.39.46; Rigaku Oxford Diffraction, 2015) was used for recording reflections and preliminary data reduction. Reflection intensities were corrected for the DAC absorption, sample shadowing by the gasket, the sample absorption, and reflections overlapping with diamond reflections were eliminated (*CrysAlisPro*). *OLEX2-1.2* (Dolomanov *et al.*, 2009), *SHELXL* (Sheldrick, 2015a) and *SHELXT* (Sheldrick, 2015b) were used to solve the structures by direct methods, and to refine the models by full matrix least-squares. Anisotropic displacement factors were applied for non-hydrogen atoms. The H atoms were located from the molecular geometry, with the C—H distance equal to 0.93 Å in pyridazine and 0.97 Å in the methyl groups, and their U_{iso} factors constrained to 1.2 and 1.5 times U_{eq} of the carriers, respectively. The site occupancy factor (SOF) of
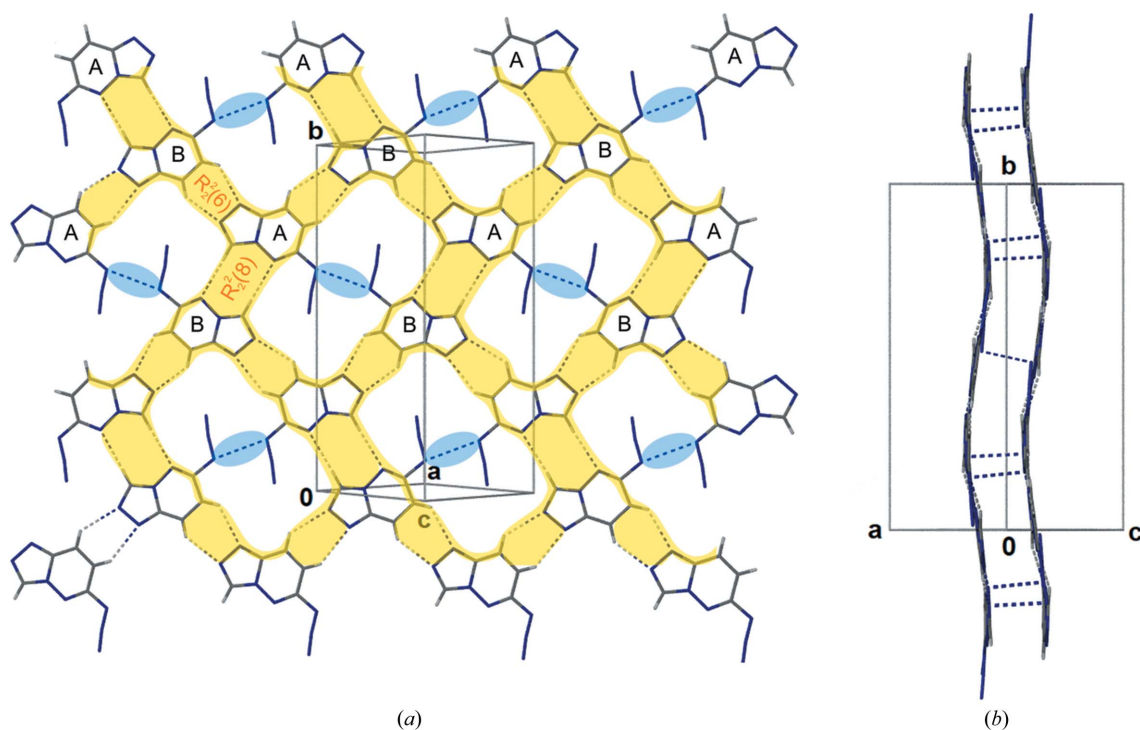

(a)   (b)

Figure 4
The crystal structure of $C_5H_3N_7$: (*a*) one hydrogen-bonded sheet extending along plane (10$\bar{1}$); and (*b*) two neighboring sheets projected along the diagonal direction [101]. The pattern of CH···N bonds is highlighted yellow and contacts N···N between the azide groups are highlighted blue. Letters A and B label independent molecules (*cf.* Fig. S3).

the oxygen atoms of water molecules in $C_6H_5N_7 \cdot xH_2O$ was freely refined and then fixed in the final cycles, in order to avoid the correlation between the SOF and the atomic displacement parameters. The crystal data and refinement details are summarized in Tables 1 and Tables S1–S3; the experimental and structural details have been deposited in the Cambridge Structural Database with CCDC numbers 2021837–2021846 for $C_5H_3N_7$ and 2021847–2021854 for $C_6H_5N_7$. Structural drawings have been prepared using the *X-Seed* interface of *POV-Ray* (Barbour, 2001; Persistence of Vision Raytracer, 2004) and *Mercury* (Macrae *et al.*, 2020).

3. Results and discussion

The crystal structures formed of molecules $C_5H_3N_7$ and $C_6H_5N_7$ are considerably different and they both are stable in all the temperature and pressure ranges investigated in this study. The $C_5H_3N_7$ crystal is monoclinic, with two symmetry-independent molecules (*A* and *B*). Compound $C_6H_5N_7$ crystallizes in the form of a tetragonal hydrated clathrate. Its structure consists of molecules CH$\cdots$N bonded into the host framework with pores running down [**z**]. The pores contain strongly disordered water molecules. Different patterns of CH$\cdots$N bonded molecules are present in the structures. It is also characteristic of the $C_5H_3N_7$ and $C_6H_5N_7 \cdot xH_2O$ structures that the azide substituents group together; their shortest N$\cdots$N intermolecular distances are 3.131 (4) Å and

3.202 (3) Å, respectively, under ambient conditions (Figs. 4 and 5).

The topology of the CH$\cdots$N patterns is considerably different in $C_5H_3N_7$ and $C_6H_5N_7$. In $C_5H_3N_7$, the CH$\cdots$N bonds link the molecules into wavy sheets with confined small regions of N$\cdots$N contacts between azide groups, as illustrated in Fig. 4. The sheets run along crystallographic plane (10$\bar{1}$) and their 'wavevector' points along [**y**]. Interestingly, the sheets display the crystallographic symmetry: translations [**a**+**c**] and [**b**], screw axis 2_1, parallel to [**y**]. Besides, there are pseudo-symmetries of inversion centers between molecules *A* and *B*, at the midpoints between the azide groups and at the center of the $R_2^2(8)$ ring (Etter *et al.*, 1990) and a pseudo-glide plane *n* perpendicular to [**y**]. The most significant departure from the pseudo-inversion center is due to the inclination angle of 7.34 (9)° (at normal conditions) between molecules *A* located on the maxima/minima of corrugated sinusoidal sheets and molecules *B* located on their slopes (Fig. 4). The neighboring sheets are related by genuine inversion centers, and pairs of the sheets are related through glide planes *c* (*cf.* Fig. S1).

In $C_6H_5N_7 \cdot xH_2O$ there are three distinct types of interaction regions (Fig. 5). The most prominent region consists of CH$\cdots$N bonds linking the $C_6H_5N_7$ molecules into a three-dimensional framework. Two other regions, one consisting of contacts N$\cdots$N and the other one potentially capable of forming bonds OH$\cdots$O, OH$\cdots$N and CH$\cdots$O (the short contacts present in the structure involve disordered water molecules, for which we could not locate the H atoms in this
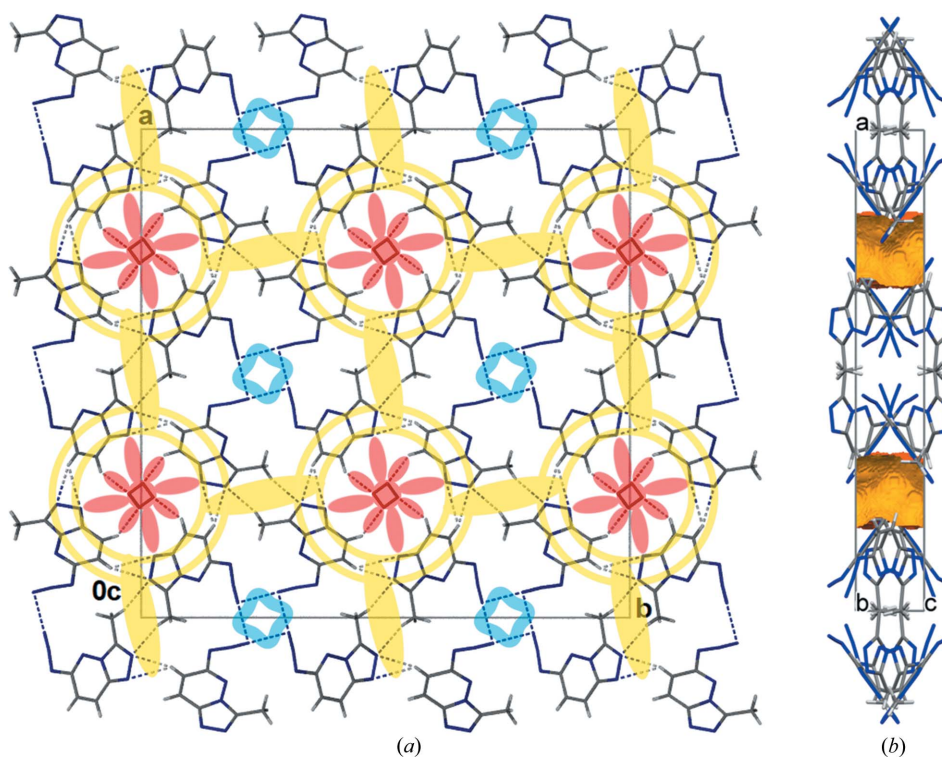

(*a*)	(*b*)

Figure 5
Structure of $C_6H_5N_7 \cdot 0.5H_2O$ at 0.58 GPa/296 K: (*a*) projected down [**z**] with the regions of CH$\cdots$N bonds highlighted yellow, contacts N$\cdots$N blue, and short OH$\cdots$O, OH$\cdots$N and CH$\cdots$O light red (*cf.* Fig. S4); and (*b*) the [**x**] projection with the solvent accessible volume of the pores shown in orange, as calculated with probe radius equal 1.2 Å and grid spacing 0.1 Å.

Anna Olejniczak *et al.* · Azido-triazolopyridazines **1139**

study) are both in the form of helical columns running down 4_1 screw axes parallel to [**z**] in the CH$\cdots$N bonded framework. The disordered water molecules are contained in the channel pores parallel to [**z**] (Fig. 5 and Fig. S2). The pores are quite wide and the water molecules can move along [**z**] and the crystal can change their contents, consistent with the results of high-pressure experiments described below. The voids occupy 6.5% of the crystal volume (assessed for the probing sphere of 1.2 Å in diameter) and they can accommodate spheres of maximum radius 1.66 Å; the translational parameter along these pores is quite short ($a/4$, see Table 1) and there are no narrow parts in the pores.

In both compounds the molecules are present in the form of azido-triazole tautomer. The shortest intermolecular contacts CH$\cdots$N, N$\cdots$N and CH$\cdots$O (Fig. 6) may be associated with the main cohesion forces under ambient conditions. The Hirshfeld fingerprint plots (Fig. 6 and Fig. S5) confirm that the shortest contacts are those of CH$\cdots$N hydrogen bonds (the spikes in the plots), while the N$\cdots$N distances are less exposed in the central part of the fingerprints. These features are common for both independent molecules in $C_5H_3N_7$ and for the molecule of $C_6H_5N_7 \cdot xH_2O$. The N$\cdots$N distances observed in $C_5H_3N_7$ and $C_6H_5N_7 \cdot xH_2O$ are similar to those observed in both polymorphs of analogs compound 6-azido-1,2,3,4-tetrazolo[1,5-*b*]pyridazine ($C_4H_2N_8$) (Olejniczak *et al.*, 2019), however, the topologies of CH$\cdots$N and N$\cdots$N regions in $C_4H_2N_8$ are different. In both polymorphs of $C_4H_2N_8$ clearly defined sheets of CH$\cdots$N and N$\cdots$N regions are present.

The conformation of the azide groups is characteristic of the 6-substituted pyridazine rings, with the torsion angle N5—C6—N10—N11 of about 3 (3)° (molecule *A*) and 5 (3)° (molecule *B*) in $C_5H_3N_7$ and 4.5 (1.5)° in $C_6H_5N_7 \cdot xH_2O$. We have not noted any significant systematic changes in the N—N

bond lengths in the azide groups, which in principle can transform between −N═N$^+$═N$^-$ and −N$^-$—N$^+$≡N configuration. Bond angle N10—N11—N12 is of about 170 (2)°, bent in the direction opposite to angle C6—N10—N11.

The intermolecular distances in $C_5H_3N_7$ are gradually compressed at a similar rate for CH$\cdots$N and N$\cdots$N contacts (Fig. S6). This result is consistent with the 2D pattern of CH$\cdots$N bonds in the sheets, with 'islands' of N$\cdots$N interactions. The intermolecular distances CH$\cdots$N in $C_6H_5N_7 \cdot xH_2O$ initially increase at 0.1 GPa (Fig. S7), which is consistent with the increased volume due to the uptake of water molecules into pores.

The compression of $C_5H_3N_7$ is typical for a molecular crystal, monotonically reduced in size in all directions (Fig. 7 and Fig. S8). This crystal compared to $C_4H_2N_8$ (Olejniczak *et al.*, 2019) is harder: compressibility $\beta = -1/V \cdot \partial V/\partial p$ at 0.40 GPa for phase α-$C_4H_2N_8$ is 0.102 GPa^{-1} and at 0.49 GPa for phase β-$C_4H_2N_8$ is 0.085 GPa^{-1} versus the compressibility of $C_5H_3N_8$ at 0.54 GPa equal to 0.072 GPa^{-1}. This difference can be attributed to a larger contribution of CH$\cdots$N bonds to the cohesion forces in $C_5H_3N_7$ than in $C_4H_2N_8$.

The compression of $C_6H_5N_7 \cdot xH_2O$ and thermal expansion of this crystal is shown in Fig. 8 (*cf.* Fig. S9). The thermal expansion in all 300–100 K range is nearly linear and the volume contracts to about 97%, as expected for an average molecular crystal. The linear expansion plots along [**x**] and [**y**] are weakly convex ($\partial^2 a/\partial T^2$ is positive), while the expansion along [**z**] is weakly concave ($\partial^2 c/\partial T^2 < 0$). This feature corresponds to the strongly anisotropic structure, with pores parallel to [**z**] and perpendicular to [**x**] and [**y**].

The volume compressibility of $C_6H_5N_7$ is clearly anomalous in the 0.1 MPa to 0.1 GPa pressure region, the line fitted to the volume values measured between 0.1 and 0.58 GPa clearly
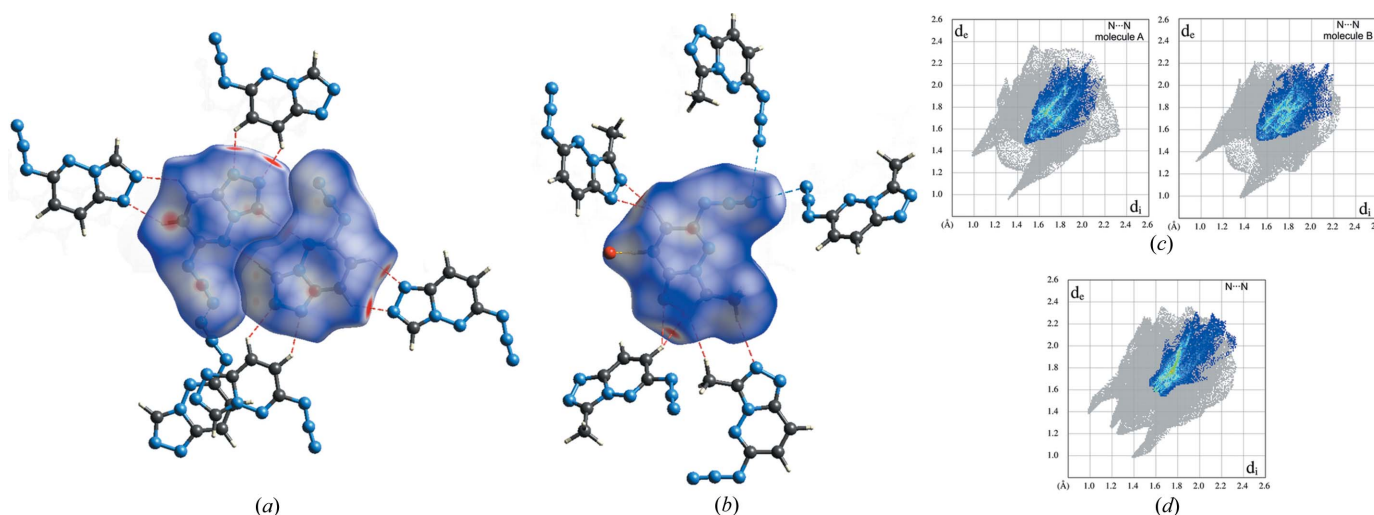

Figure 6
Hirshfeld surfaces decorated with the color scale depending on the normalized contact distances: (*a*) in $C_5H_3N_7$ at 0.85 GPa/296 K, (*b*) in $C_6H_5N_7 \cdot 0.6H_2O$ at 0.23 GPa/296 K; (*c*) the fingerprint plots of independent $C_5H_3N_7$ molecules *A* and *B* at 0.85 GPa/296 K and (*d*) the fingerprint plot of $C_6H_5N_7 \cdot 0.6H_2O$ molecule at 0.23 GPa/296 K (*cf.* Fig. S5). The surface regions forming intermolecular contacts equal to the sum of their van der Waals radii (Bondi, 1964) are white, shorter - red and longer - blue. The drawings include the neighboring molecules involved in short contacts.

points above the volume at 0.1 MPa, by about 2 Å³ per formula unit. This effect can be attributed to an intake of the molecules from the hydrostatic medium into the pores. It is plausible that the pressure pushes additional molecules into the pores, which causes an initial increase of the crystal volume. This effect is also clearly seen in the linear compression along [**x**] and [**y**]. An average volume of one water molecule in hydrates is of about 22.8 Å³ (Glasser, 2019), so it can be estimated that the contents of water in $C_6H_5N_7 \cdot xH_2O$ crystal increases by about 0.1 H_2O per formula unit. Hence the composition of the $C_6H_5N_7 \cdot xH_2O$ crystal changes and therefore the measurements of the unit-cell dimensions as a function of pressure are not the one-compound crystal compression in the strictly physical sense. According to the X-ray diffraction data refinements in the 0.1 MPa–0.1 GPa range the x parameter in $C_6H_5N_7 \cdot xH_2O$ changes from 0.3 to 0.6.

Figure 8
Unit-cell dimensions (*a*) and molecular volume (*b*) of $C_6H_5N_7 \cdot xH_2O$ as a function of temperature (open symbols) and pressure (full symbols). The dotted lines indicate the pressure region involving the H_2O transport into the pores (*cf.* Fig. S9). Where not indicated, the estimated standard deviations are smaller than the plotted symbols.

4. Conclusions

The increased number of H-atom donors in two high-nitrogen-contents 6-azido-1,2,4-triazolo[4,3-*b*]pyridazine, ($C_5H_3N_7$), and its methyl derivative ($C_6H_5N_7$) drastically changed the topology of CH···N and N···N contacts, compared to the previously studied 6-azido-1,2,3,4-tetrazolo[1,5-*b*]pyridazine ($C_4H_2N_8$) polymorphs. The CH groups in $C_5H_3N_7$ and $C_6H_5N_7$ are effectively involved in CH···N bonds, binding the molecules into frameworks. It is characteristic that none of these CH···N bonds involve the azide groups, which form short contacts between themselves. All of these N···N contacts are longer than double the van der Waals radius of the nitrogen atom. It appears that the contribution of azide groups to the cohesion forces is very weak. The strong contribution of hydrogen bonds CH···N to cohesion forces is supported by the formation of the porous framework in $C_6H_5N_7$ capable of the sorption of water under ambient and high-pressure conditions.
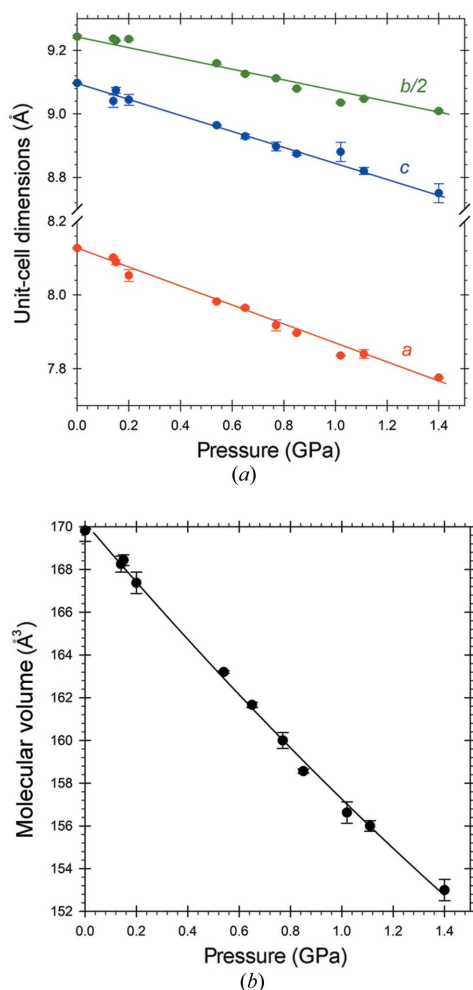

Figure 7
Compression of the unit-cell dimensions (*a*) and molecular volume (*b*) of $C_5H_3N_7$. Straight lines have been fitted to the lengths and polynomial function $V = 170.20 - 14.31p + 1.33p^2$ to the volume (*cf.* Fig. S8). Where not indicated, the estimated standard deviations are smaller than the plotted symbols.
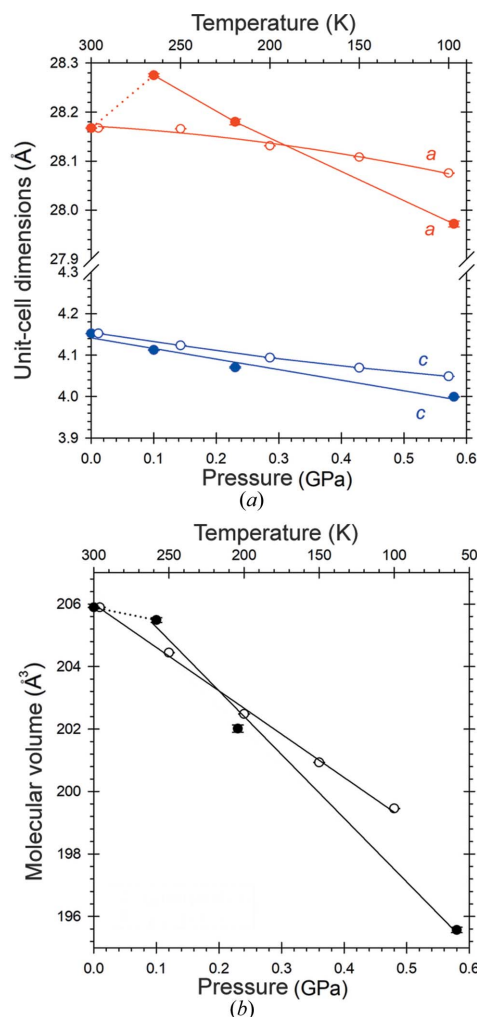
research papers

References

Bałoniak, S. & Katrusiak, A. (1994). *Pol. J. Chem.* **68**, 683–691.
Barbour, L. J. (2001). *J. Supramol. Chem.* **1**, 189–191.
Bernstein, J. (2002). *IUCr Monographs on Crystallography*. Oxford: Clarendon Press.
Boldyreva, E. V. (2008). *Acta Cryst.* A**64**, 218–231.
Boldyreva, E. V. (2014). *Z. Kristallogr.* **3**, 236–245.
Bondi, A. (1964). *J. Phys. Chem.* **68**, 441–451.
Budzianowski, A. & Katrusiak, A. (2004). *High-Pressure Crystallography*, edited by A. Katrusiak and P. F. McMillan, pp. 101–112. Dordrecht: Kluwer.
Dolomanov, O. V., Bourhis, L. J., Gildea, R. J., Howard, J. A. K. & Puschmann, H. (2009). *J. Appl. Cryst.* **42**, 339–341.
Etter, M. C., MacDonald, J. C. & Bernstein, J. (1990). *Acta Cryst.* B**46**, 256–262.
Fabbiani, F. P. A. & Pulham, C. R. (2006). *Chem. Soc. Rev.* **35**, 932–942.
Gatta, G. D., Lotti, P. & Tabacchi, G. (2018). *Phys. Chem. Miner.* **45**, 115–138.
Gaydamaka, A. A., Arkhipov, S. G., Zakharov, B. A., Seryotkin, Y. V. & Boldyreva, E. V. (2019). *CrystEngComm*, **21**, 4484–4492.
Glasser, L. (2019). *Acta Cryst.* B**75**, 784–787.
Katrusiak, A. A., Bałoniak, S. & Katrusiak, A. S. (1996). *Pol. J. Chem.* **70**, 1279–1289.
Katrusiak, A., Skierska, U. & Katrusiak, A. (2005). *J. Mol. Struct.* **751**, 65–73.
Macrae, C. F., Sovago, I., Cottrell, S. J., Galek, P. T. A., McCabe, P., Pidcock, E., Platings, M., Shields, G. P., Stevens, J. S., Towler, M. & Wood, P. A. (2020). *J. Appl. Cryst.* **53**, 226–235.
Mao, H. K., Xu, J. & Bell, P. M. (1985). *J. Geophys. Res.* **91**, 4673–4676.
Merrill, L. & Bassett, W. A. (1974). *Rev. Sci. Instrum.* **45**, 290–294.
Millar, D. I. A., Marshall, W. G., Oswald, I. D. H. & Pulham, C. R. (2010). *Cryst. Rev.* **16**, 2, 115–132.
Olejniczak, A., Katrusiak, A., Podsiadło, M. & Katrusiak, A. (2019). *Cryst. Growth Des.* **19**, 1832–1838.
Persistence of Vision (2004). *Persistence of Vision Raytracer*, Version 2.6. Persistence of Vision Pty. Ltd, Williamstown, Victoria, Australia.
Piermarini, G. J., Block, S., Barnett, J. D. & Forman, R. A. (1975). *J. Appl. Phys.* **46**, 2774–2780.
Resnati, G., Boldyreva, E., Bombicz, P. & Kawano, M. (2015). *IUCrJ*, **2**, 675–690.
Rigaku Oxford Diffraction (2015). *CrysAlisPro* Software System. Rigaku Oxford Diffraction, Yarnton, UK. http://www.rigaku.com.
Seryotkin, Y. V., Dement'ev, S. N. & Ancharov, A. I. (2016). *J. Struct. Chem.* **57**, 1386–1391.
Sheldrick, G. M. (2015a). *Acta Cryst.* A**71**, 3–8.
Sheldrick, G. M. (2015b). *Acta Cryst.* C**71**, 3–8.
Yang, J., Gong, X. & Wang, G. (2015). *RSC Adv.* **5**, 9503–9509.
Zakharov, B. A., Gribov, P. A., Matvienko, A. A. & Boldyreva, E. V. (2017). *Z. Kristallogr.* **232**, 751–757.